Electronic Supplementary Material (ESI) for Inorganic Chemistry Frontiers.

Supporting Information

Dynamic Mechanical Equilibrium of Silicon Anodes for Lithium-ion Batteries Enabled by Surface Hydroxyl-Rich Bonding

Fangfang Zhao,[a] Bowen Tao,[c] Liming Yu,[a] Cong Pan,[b] Lei Ma,[a] Liangming Wei,*[a]*

Gen Tang,[c] Yue Wang [c] and Xiang Guo[c]*

[a] *Key Laboratory for Thin Film and Microfabrication of Ministry of Education, Department of Micro/Nano Electronics, School of Electronic Information and Electrical Engineering, Shanghai Jiao Tong University, 800 Dongchuan RD, Minhang District, Shanghai, 200240, China*

[b] *College of Data Science, Jiaxing University, No.899 Guangqiong Road, Jiaxing City, Zhejiang Province, China*

[c] *National Key Laboratory of Aerospace Chemical Power, Hubei Institute of Aerospace Chemotechnology, Xiangyang, 441003, Hubei, China*

**Corresponding author. Tel./fax: +86-21-34205665,*

E-mail: lmwei@sjtu.edu.cn, Shanghai Jiao Tong University, 800 Dongchuan RD, Minhang District, Shanghai, 200240, China.

1. Lithium-ion diffusion coefficient calculation

The lithium-ion diffusion coefficient (D) was obtained using Equation 1.[1] The parameter R represents the gas constant, T is absolute temperature, A is the electrode surface area, n is the number of electrons involved in electron transfer reactions in each molecule, F is the Faraday constant, C is the concentration of Li^+ in Si electrode and σ_ω is Warburg factor got from the slope of the line $Z' \sim \omega^{1/2}$ in Figure 5d, respectively.

$$D = (R^2T^2)/(2A^2n^4F^4C^2\sigma_\omega^2) \quad (1)$$

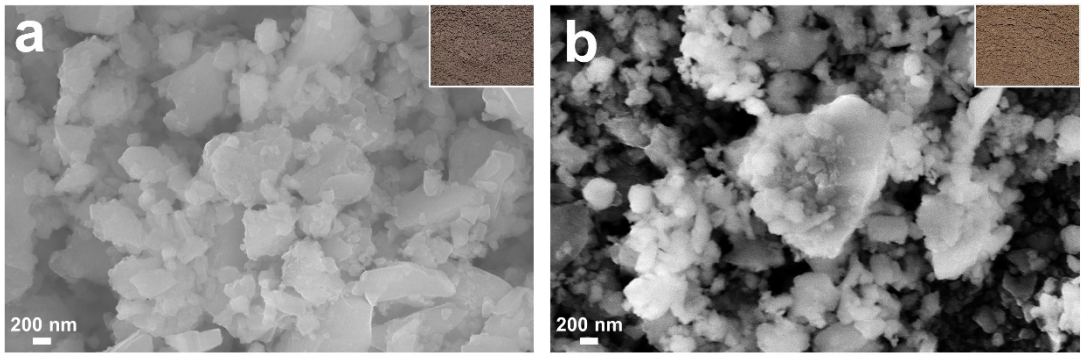

Figure S1. SEM images for (a) Si-$C_{11}H_{24}$ and (b) Si-H_2O. Their photographs are represented in the insets.

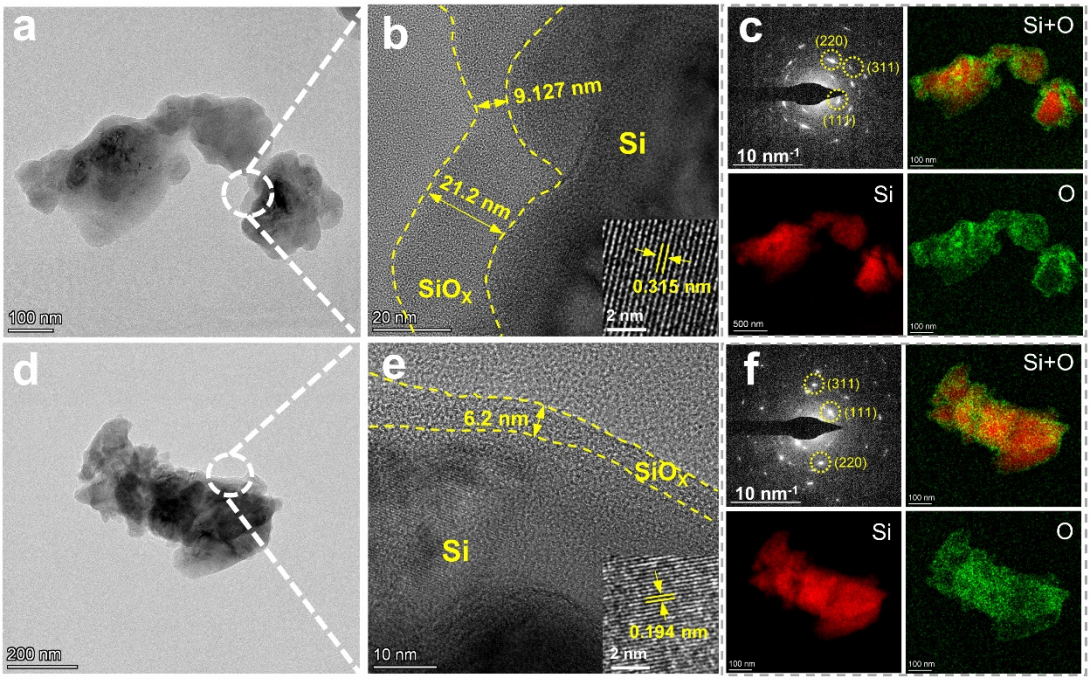

Figure S2. TEM images for (a) Si-H_2O and (d) Si-$C_{11}H_{24}$. HRTEM images for (b) Si-H_2O and (e) Si-$C_{11}H_{24}$. SAED pattern, all element, Si, and O scanning TEM/energy dispersive spectroscopy (EDS) elemental mapping of the (c) Si-H_2O and (f) Si-$C_{11}H_{24}$.

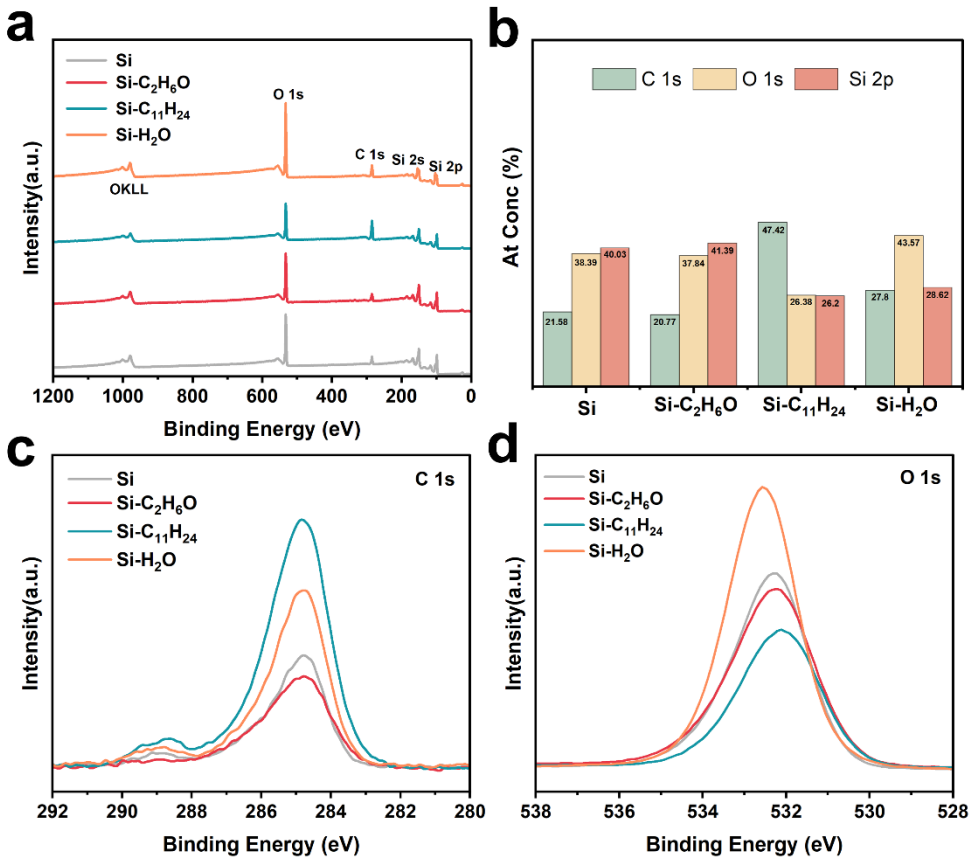

Figure S3. (a) XPS survey spectra and (b) the element atomic concentration (%) of the samples; XPS spectra of the (c) C 1s and (d) O 1s.

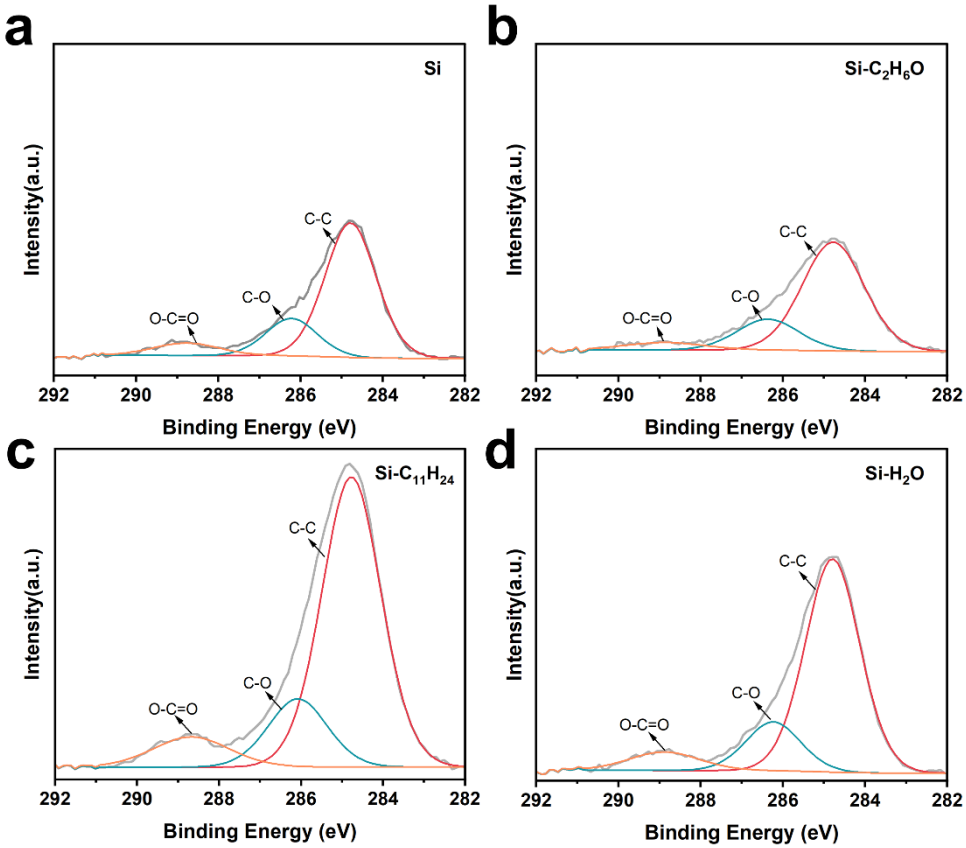

Figure S4. XPS spectra of the C 1s for (a) Si, (b) Si-C_2H_6O, (c) Si-$C_{11}H_{24}$, and (d) Si-H_2O;

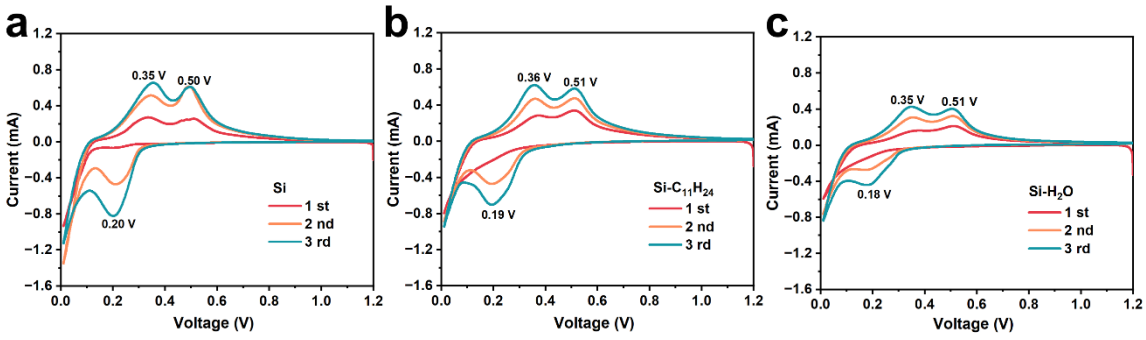

Figure S5. CV curves of (a) Si, (b) Si-$C_{11}H_{24}$, and (c) Si-H_2O.

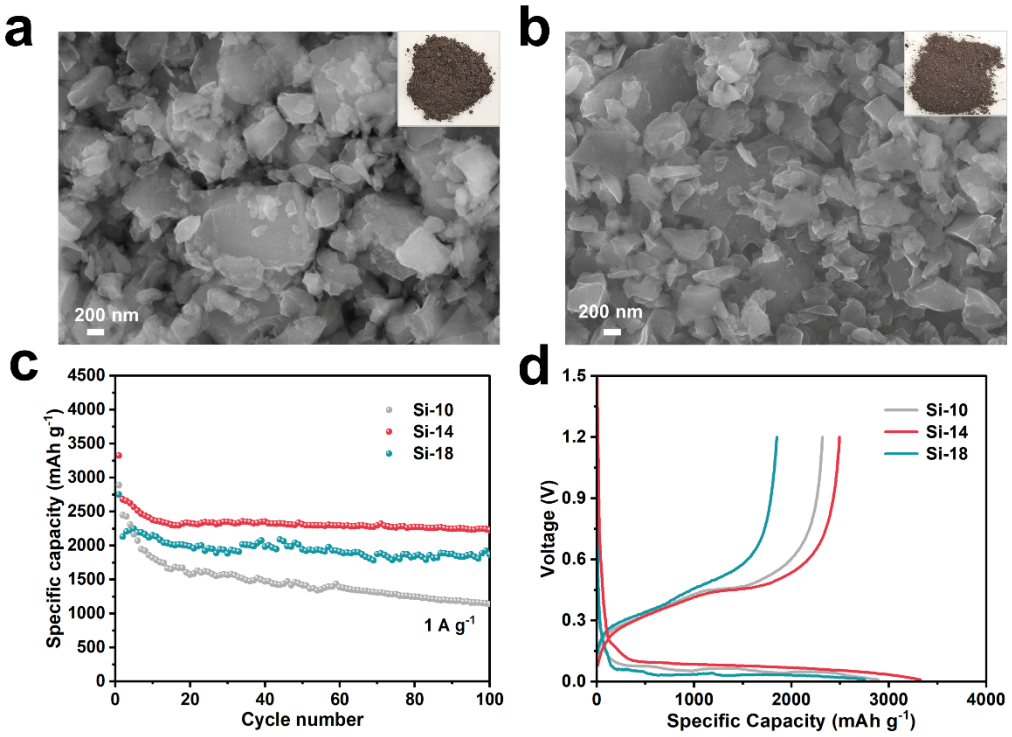

Figure S6. SEM images of (a) Si-10 and (b) Si-18. Their photographs are represented in the insets. (c) the cycle performance at 1 A g^{-1} and (d) the charge-discharge curve for the first cycle of Si-10, Si-14, and Si-18.

The ball-to-powder mass ratio plays a critical role in ball milling, and its influence on final product quality has been investigated from the outset.[2] Lower ratios (Figure S6a) may result in inadequate milling effectiveness and the presence of larger particles, while excessive ball-to-powder mass ratio (Figure S6b) tends to cause nanoparticle aggregation. As shown in Figure S6c, Si-14 exhibits a significant advantage over Si-10 and Si-18 in capacity retention and cycling stability. Low discharge potentials (below 30-65 mV) facilitate the formation of crystalline $Li_{15}Si_4$.[3] The repeated transformation between crystalline $Li_{15}Si_4$ and amorphous Li_xSi during the repeated charge/discharge process leads to capacity deterioration.[4] According to Figure S6d, Si-14 presents a sloped charge-discharge platform, whereas Si-10 and Si-18 experience abrupt discharge

voltage drops, indicating greater voltage polarization than Si-14. This implies that the increased formation of crystalline $Li_{15}Si_4$ and severe polarization results in continuous battery capacity decline. Thus, the optimal ratio is determined to be 14:1.

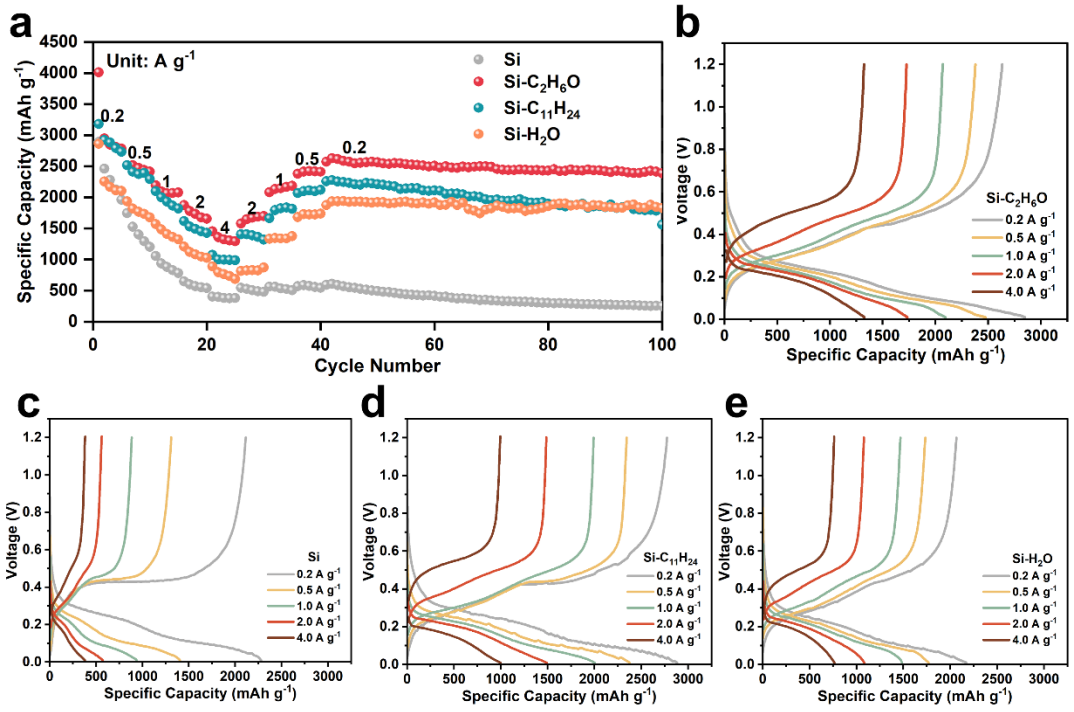

Figure S7. (a) Rate performance of the samples; The charge-discharge profiles of (b) Si-C_2H_6O, (c) Si, (d) Si-$C_{11}H_{24}$, and (e) Si-H_2O at different rates based on (a).

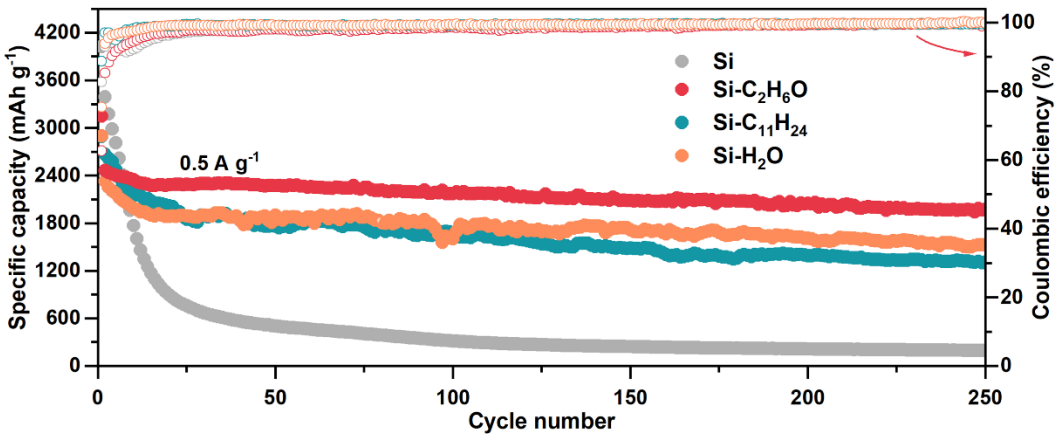

Figure S8. cycling performance at 0.5 A g^{-1} of Si, Si-C_2H_6O, Si-$C_{11}H_{24}$, and Si-H_2O.

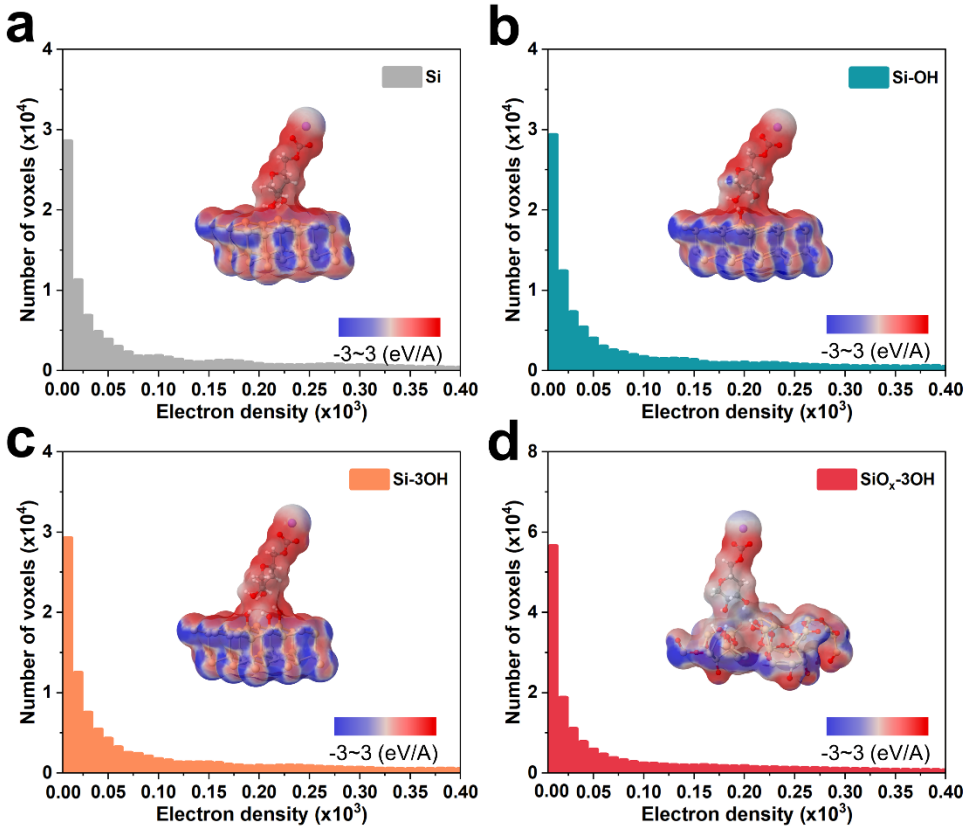

Figure S9. The number of voxels distribution near the interface between different silicon surfaces and CMC. The inserts are the electrostatic potential distribution of (a) Si, (b) Si-OH, (c) Si-3OH, and (d) SiO_x-3OH.

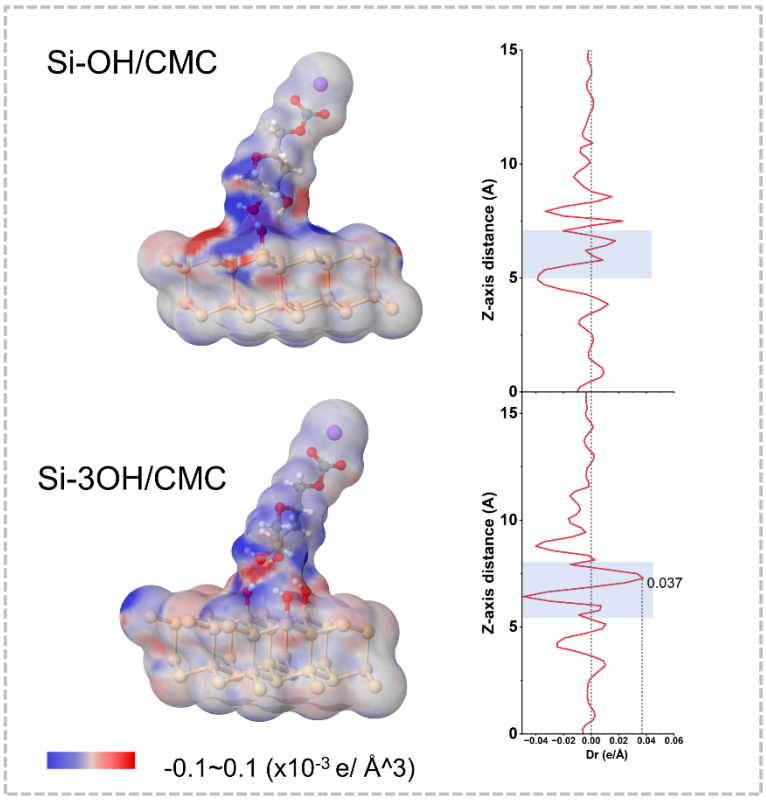

Figure S10. Charge density difference for CMC on the surface of Si-OH and Si-3OH, with isosurface level set to 1x10^{-3} e Å $^{-3}$.

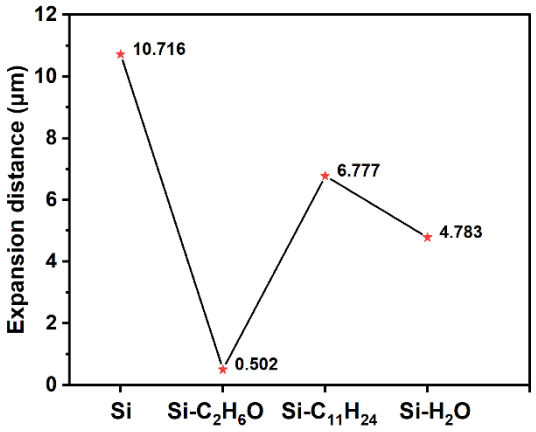

Figure S11. Cross-sectional gap of the electrode before and after 50 cycles.

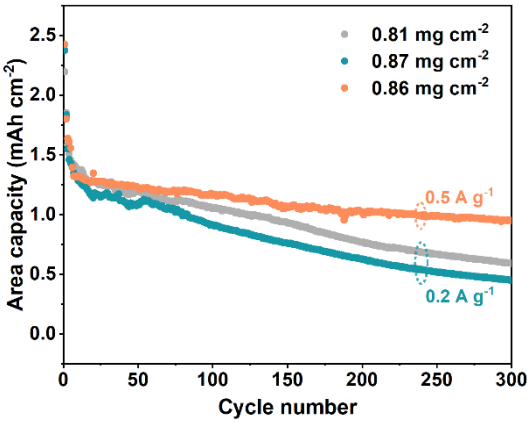

Figure S12. The cycling performance of the Si-C_2H_6O anodes at different current densities when the mass ratio of Si/acetylene black/CMC is 8:1:1.

By adjusting the mass ratio of Si/acetylene black/CMC to 8:1:1, the Si-C_2H_6O anode with an areal mass load of 0.86 mg cm^{-2} can maintain an area capacity of 0.95 mAh cm^{-2} at 0.5 A g^{-1} after 300 cycles. The capacity retention is lower at 0.2 A g^{-1} at a similar areal mass loading. Overall, when the mass ratio of Si/acetylene black/CMC is 8:1:1, the electrode demonstrates a higher initial discharge capacity but an inferior performance (Figure S12). The excessive silicon content may increase the electrolyte's contact area, leading to continuous electrolyte decomposition and electrode capacity loss. Future improvements may require carbon coating for better results.

Table S1. XPS data for the C 1s core level spectra measured on samples.

samples	Assignment binding energy (eV)	Assignment	Concentration (%)
Si	284.8	C-C	71.4
	286.2	C-O	20.0
	288.8	O-C=O	8.60
$Si-C_2H_6O$	284.8	C-C	72.6
	286.4	C-O	20.8
	288.8	O-C=O	6.60
$Si-C_{11}H_{24}$	284.8	C-C	72.9
	286	C-O	17.2
	288.7	O-C=O	9.90
$Si-H_2O$	284.8	C-C	74.5
	286.2	C-O	17.1
	288.8	O-C=O	8.40

Table S2. Specific capacity of electrodes with different cycles at 0.5 A g^{-1} and 1 A g^{-1}.

	0.5 A g^{-1}			1 A g^{-1}		
	2nd (mAh g^{-1})	250th (mAh g^{-1})	Capacity retention	2nd (mAh g^{-1})	500th (mAh g^{-1})	Capacity retention
Si	3393.8	197.8	6%	2250.2	67.4	3%
$Si-C_2H_6O$	**2466.2**	**1972.9**	**80%**	**3054.2**	**2041.8**	**67%**
$Si-C_{11}H_{24}$	2671.7	1307.8	49%	2615	745.4	29%
$Si-H_2O$	2329.7	1527.5	66%	2281.8	1201.7	53%

Table S3. Comparison of the cycling performance of different anodes utilizing hydrogen bonding.

Ref.	Material/ Binder	Capacity retention	Rate performance
5	Nano Si/ PMDOPA-20	~1600 mAh g^{-1} after 520 cycles at 840 mA g^{-1}	~700 mAh g^{-1} at 4.2 A g^{-1}
6	Nano Si/ NaPAA-*g*-CMC	1816 mAh g^{-1} after100 cycles at 840 mA g^{-1}	~900 mAh g^{-1} at 3.36 A g^{-1}
7	Nano Si/ DG5	over 1000 mAh g^{-1} after 150 cycles under 0.5C.	~1200 mAh g^{-1} at 4.2 A g^{-1}
8	Nano Si/ ESVCA	1786 mAh g^{-1} after 200 cycles at 500 mA g^{-1}	1633 mAh g^{-1} at 4 A g^{-1}
9	Nano Si/ PAA/PANI IPA	2205 mAh g^{-1} after 300 cycles at 420 mA g^{-1}	1091.4 mAh g^{-1} at 10 C
10	(PDA/GO-Si)/PVDF	1300 mAh g^{-1} after 450 cycles at 500 mA g^{-1}	~500 mAh g^{-1} at 1 A g^{-1}
11	Sio /PAA	1540.8 mAh g^{-1} after 150 cycles at 200 mA g^{-1}	~1400 mAh g^{-1} at 1C
12	Nano Si/ TA-c-PAA	1742 mAh g^{-1} after 450 cycles at 1 A g^{-1}	1599 mAh g^{-1} at 2 C
Our work	Si-C_2H_6O/ CMC	2041 mAh g^{-1} after 500 cycles at 1 A g^{-1}	1325 mAh g^{-1} at 4 A g^{-1}

References

1. L. Ma, X. Fu, F. Zhao, W. Su, L. Yu, C. Lu, L. Wei, G. Tang, Y. Wang and X. Guo, High-performance carboxymethyl cellulose integrating polydopamine binder for silicon microparticle anodes in lithium-ion batteries, *ACS Appl. Energy Mater.*, 2023, **6**, 1714-1722.
2. M. Cabello, E. Gucciardi, A. Herran, D. Carriazo, A. Villaverde and T. Rojo, Towards a high-power Si@graphite anode for lithium ion batteries through a wet ball milling process, *Molecules*, 2020, **25**.
3. M. N. Obrovac and L. Christensen, Structural changes in silicon anodes during lithium insertion/extraction, *Electrochem Solid St*, 2004, **7**, A93.
4. S. Misra, N. Liu, J. Nelson, S. S. Hong, Y. Cui and M. F. Toney, In situ X-ray diffraction studies of (de)lithiation mechanism in silicon nanowire anodes, *ACS Nano*, 2012, **6**, 5465-5473.
5. D. Yao, J. Feng, J. Wang, Y. Deng and C. Wang, Synthesis of silicon anode binders with ultra-high content of catechol groups and the effect of molecular weight on battery performance, *J. Power Sources*, 2020, **463**, 228188.

6. L. Wei, C. Chen, Z. Hou and H. Wei, Poly (acrylic acid sodium) grafted carboxymethyl cellulose as a high performance polymer binder for silicon anode in lithium ion batteries, *Sci. Rep.*, 2016, **6**, 19583.
7. B. Koo, H. Kim, Y. Cho, K. T. Lee, N.-S. Choi and J. Cho, A highly cross-linked polymeric binder for high-performance silicon negative electrodes in lithium ion batteries, *Angew Chem Int Edit*, 2012, **51**, 8762-8767.
8. S. Hu, L. Wang, T. Huang and A. Yu, A conductive self-healing hydrogel binder for high-performance silicon anodes in lithium-ion batteries, *J. Power Sources*, 2020, **449**, 227472.
9. X. Yu, H. Yang, H. Meng, Y. Sun, J. Zheng, D. Ma and X. Xu, Three-dimensional conductive gel network as an effective binder for high-performance si electrodes in lithium-ion batteries, *ACS Appl. Mater. Interfaces*, 2015, **7**, 15961-15967.
10. J. Wu, W. Tu, Y. Zhang, B. Guo, S. Li, Y. Zhang, Y. Wang and M. Pan, Poly-dopamine coated graphite oxide/silicon composite as anode of lithium ion batteries, *Powder Technol* 2017, **311**, 200-205.
11. C. Li, T. Shi, D. Li, H. Yoshitake and H. Wang, Effect of surface modification on electrochemical performance of nano-sized Si as an anode material for Li-ion batteries, *RSC Adv.*, 2016, **6**, 34715-34723.
12. J. Chen, Y. Li, X. Wu, H. Min, J. Wang, X. Liu and H. Yang, Dynamic hydrogen bond cross-linking binder with self-healing chemistry enables high-performance silicon anode in lithium-ion batteries, *J. Colloid Interface Sci.*, 2024, **657**, 893-902.